Femtotesla Direct Magnetic Gradiometer Using a Single Multipass Cell

V.G. Lucivero,[*,†] W. Lee, N. Dural, and M.V. Romalis
Department of Physics, Princeton University, Princeton, New Jersey 08544, USA

(Received 28 September 2020; revised 2 December 2020; accepted 2 December 2020; published 6 January 2021)

We describe a direct gradiometer using optical pumping with opposite circular polarization in two ^{87}Rb atomic ensembles within a single multipass cell. A far-detuned probe laser undergoes a near-zero paramagnetic Faraday rotation due to the intrinsic subtraction of two contributions exceeding 3.5 rad from the highly polarized ensembles. We develop analysis methods for the direct gradiometer signal and measure a gradiometer sensitivity of 10.1 fT/cm$\sqrt{\text{Hz}}$. We also demonstrate that our multipass design, in addition to increasing the optical depth, provides a fundamental advantage due to the significantly reduced effect of atomic diffusion on the spin-noise time-correlation, in excellent agreement with the theoretical estimate.

DOI: 10.1103/PhysRevApplied.15.014004

I. INTRODUCTION

Operation of sensitive magnetic sensors in an unshielded environment, including Earth's magnetic field and ambient noise, requires robust subtraction of common-mode magnetic signals. Environmental-noise suppression is a major challenge for several applications, such as noninvasive magnetoencephalography [1] and magnetocardiography [2], magnetic anomaly detection [3], archeology [4], mineral exploration [5], and the search for unexploded ordnance [6]. The usual way of achieving high noise cancellation and sensitivity increase is to implement a magnetic gradiometer scheme. Highly sensitive gradiometers are based on optically pumped magnetometers, the most-sensitive devices to measure low-frequency magnetic fields to date [7–10], and have been developed using either a single vapor cell with a multielement photodiode in the spin-exchange-relaxation-free regime [9,10] and at finite fields [11,12] or two microfabricated [13] or cm-sized [14,15] vapor cells, reaching subfemtotesla sensitivity in a multipass configuration [16]. Another promising approach is based on an actively shielded array of optically pumped magnetometers and it has been implemented in magnetoencephalography [17]. Here we present a direct magnetic gradiometer that uses a single output with intrinsic subtraction of rotation signals from two atomic ensembles within one multipass cell. A similar approach was used before with a single-pass configuration for rf magnetometry [18] and in a cw optical gradiometer [19]. Our multipass-optical-cavity design using a three-mirror V-shaped geometry has several advantages. It uses a single probe laser beam that passes repeatedly through two atomic ensembles that are polarized in opposite directions. As a result, a subtraction between their optical rotation signals occurs, allowing direct differential measurements. The direct cancellation of Faraday rotation from highly polarized ensembles also avoids the complication of polarimeter-signal wraparound when the optical rotation exceeds $\pi/4$ radians in a multipass geometry [20]. In addition, the optical design of the V-shaped multipass cell allows the laser beams to expand and overlap on multiple passes through the atomic ensembles. This reduces diffusion broadening and increases correlation of spin measurements, unlike in previous multipass cells that used distinct nonoverlapping beams that were detrimental for possible sensitivity increase by spin squeezing [16]. At the same time, the probe laser beam in the V-shaped multipass cell remains focused on one of the mirrors, which allows the laser beam to exit the cavity after a specific number of passes, in contrast to typical standing-wave optical cavities [21]. It also simplifies signal processing in the high-density and high-polarization regime, where partial suppression of spin-exchange relaxation [22] causes highly nonlinear spin evolution [16,20].

Firstly, we describe the V-shaped-sensor design, fabrication, and working-operation mode. Then we report typical gradiometer signals with direct subtraction of Faraday-rotation contributions with multiple wrapping and we introduce two analysis methods for sensitivity optimization to decouple the contribution of the magnetic field gradient from amplitude and phase variations. We also study the fundamental spin quantum noise and we show that, by limiting atomic interaction to the region of overlapping beams with a uniform large area, the spin-noise spectrum has a nearly Lorentzian shape, whose linewidth is dominated by spin-exchange collisions rather than atomic diffusion, in contrast to prior work [16,20]. We

[*]vito-giovanni.lucivero@icfo.eu
[†]Present address: ICFO–Institut de Ciencies Fotoniques, The Barcelona Institute of Science and Technology, 08860, Castelldefels (Barcelona), Spain.

confirm this result by reporting a slower decay time of the experimental diffusion component of the spin time-correlation function relative to prior work [16], in excellent agreement with theory [23].

II. SENSOR DESIGN AND EXPERIMENTAL SETUP

The sensor, shown in Fig. 1(a), consists of three 0.5-in. convex spherical mirrors, with 100-mm radius of curvature, that are actively aligned in a V-shaped geometry to give the desired beam propagation and then anodically bonded through silicon wafers to a Pyrex plate. The probe laser is fiber coupled, linearly polarized, and focused at near-zero angle into a 170-μm hole made at the center of the front mirror. Then it expands to a beam diameter of 3.6 mm at the back mirrors, where it nearly overlaps while undergoing 60 multiple reflections between the front and back mirrors. Because of the nonzero input angle, the probe is refocused to the front mirror at different spots, in number equal to half of the total number of beam passes as shown in the infrared picture in Fig. 1(b), before exiting the cavity. To make the atoms interact with a uniform wide beam, the atomic interaction is limited to the back region, where a 2-cm-wide Pyrex cell, which encloses the back mirrors, is also bonded to the plate through a second silicon wafer. The cell has an antireflection-coated front window and is filled with pure ^{87}Rb and N_2 buffer gas at a pressure of 90 Torr. Optical-probe-beam transmission through the cavity after 60 passes is typically greater than 50%. The cell is heated with an alternating electric current in a boron nitride oven, while the temperature is monitored by a thermocouple and stabilized to 0.1 °C. The gradiometer structure stands within five mu-metal layers of magnetic shielding, as shown in Fig. 1(c), and a concentric set of cylindrical coils (not shown). These generate the main field B_z and a uniform gradient $\partial B_z/\partial y$. The experimental scheme is shown in Fig. 1(d) in a simplified sketch with 12 probe passes. We define two atomic interaction areas, addressed as top and bottom regions, where atoms are optically pumped with opposite polarization in the gradiometer operation mode with a baseline of 1.4 cm. After multiple reflections, the probe output is collimated and detected with a conventional balanced polarimeter, whose differential signal is fed into a digital oscilloscope. The pump laser is a cw diode laser, which is amplified by a tapered amplifier and tuned to the ^{87}Rb D_1 line. A pulsed regime is generated by an acousto-optic modulator, and the first-order diffracted beam is expanded and split into two parallel beams matching the atomic

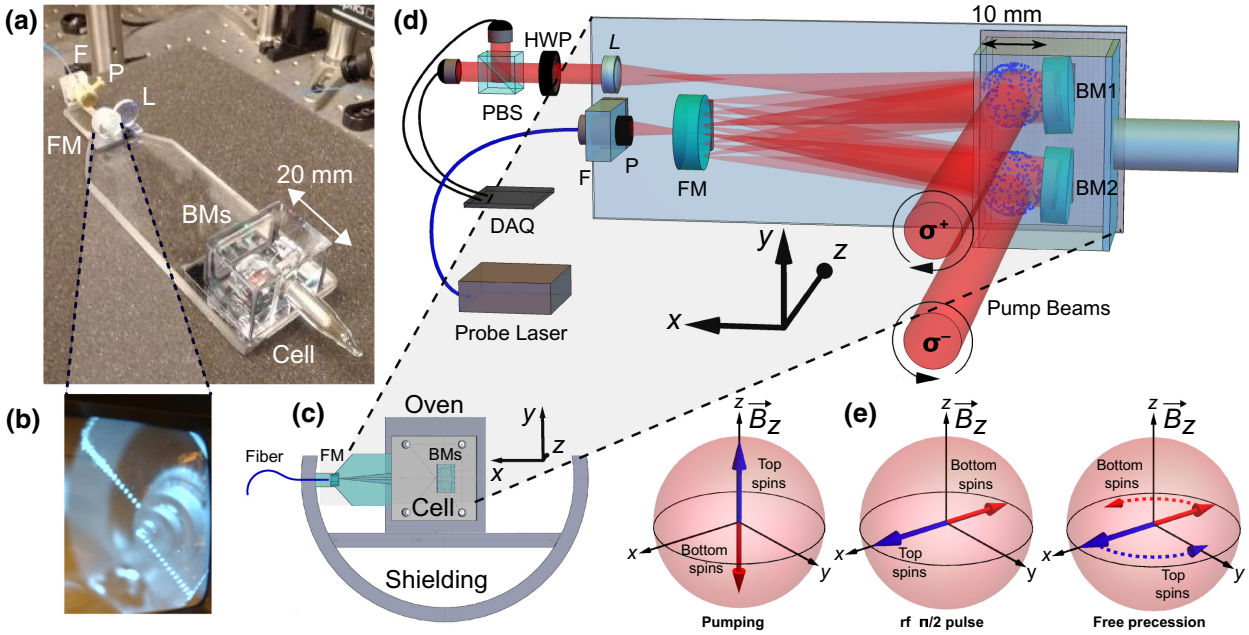

FIG. 1. (a) V-shaped cell. Image of the sensor including the probe input focuser (F) and polarizer (P), anodically bonded spherical front mirror (FM) and back mirrors (BMs), a $18 \times 20 \times 30$ mm^3 Pyrex cell enclosing both the back mirrors and the atomic vapor, and an output collimation lens (L). (b) Multipass geometry. IR image (camera not shown) of the front mirror with probe-beam spots after 60 passes through atomic ensembles before exiting the cavity. (c) Layout. Cross-section view of the V-shaped cell within a magnetic shielding with the Pyrex cell enclosed by a boron nitride oven. A magnetic field gradient is applied in the y direction, while the probe beam (input fiber coupled) and the pump beams (free space) propagate in the x and z directions, respectively, as shown in (d). (d) Full experimental sketch. DAQ, data-acquisition card; HWP, half-wave plate; PBS, polarizing beam splitter. (e) Measurement sequence. Optically induced atomic orientation for top and bottom spins, angle tilt by $\pi/2$ pulse, and free Larmor precession in the transverse plane.

interaction areas. The top and bottom pump beams are circularly polarized with opposite ellipticity, σ^+ and σ^-, by two different quarter-wave plates and are aligned along the z axis to maximize the initial atomic polarization. Atoms are pumped in the $F = 2$ hyperfine state with $m_F = 2$ and $m_F = -2$ (i.e., parallel and antiparallel with respect to the main field B_z, respectively). The measurement sequence is depicted in Fig. 1(e). After 3 ms of cw optical pumping, we apply a $\pi/2$ rf pulse with 30 cycles to the B_y coil to flip the spins in the transverse plane. At this point, top and bottom spins have opposite orientation in the x direction, corresponding to a π phase difference. We also apply an out-of-phase rf pulse to the gradient coil $\partial B_x/\partial y$ to create a small phase difference in spin-precession signals for the two arms that compensates for the finite opening angle of the probe beam in the two arms of the V-shaped cell. After the $\pi/2$ pulse, the spins freely precess at the Larmor frequency $\nu_L = (\gamma/2\pi)B_z$, where $\gamma = g_F\mu_B/\hbar$ is the gyromagnetic ratio, and we continuously record the free induction decay (FID) using paramagnetic Faraday rotation of the probe laser. The entire pump-tilt-probe cycle is repeated with a driving period τ of 16.666 ms.

III. EXPERIMENTAL RESULTS AND DATA ANALYSIS

The FID output signal of the polarimeter is given by

$$V(t) = V_{\rm ver}(t) - V_{\rm hor}(t) = V_0 \sin\left\{2\phi_0^{\rm top}\sin\left[2\pi\left(\nu_L + \frac{\Delta\nu}{2}\right)t + d_0^{\rm top}\right]e^{-t/T_2^{\rm top}} - 2\phi_0^{\rm bot}\sin\left[2\pi\left(\nu_L - \frac{\Delta\nu}{2}\right)t + d_0^{\rm bot}\right]e^{-t/T_2^{\rm bot}}\right\}, \quad (1)$$

where V_0 is the voltage corresponding to full probe intensity, $\phi_0^{\rm top}$ ($\phi_0^{\rm bot}$), $d_0^{\rm top}$ ($d_0^{\rm bot}$), and $T_2^{\rm top}$ ($T_2^{\rm bot}$) are the maximum rotation [20], the phase, and the transverse relaxation time of the top (bottom) atomic ensemble [24], and $\Delta\nu$ is the difference in precession frequency due to the magnetic gradient.In Fig. 2 we report typical rotation signals $V_{\rm top}(t)$ and $V_{\rm bot}(t)$ at 120 °C, obtained by our blocking one of the two pump beams, respectively. Each contribution has a maximum rotation of about 3.5 rad, resulting in wrapping and multiple zero crossings within a Larmor period. Over a shorter timescale, the opposite initial amplitude of the two signals is evident. Then, when both pump beams are *on*, a direct subtraction occurs, as shown in the inset in Fig. 2, resulting in an amplitude cancellation greater than 98%. In Fig. 3 we show the dependence of this special direct signal on the applied uniform gradient at 100 °C, optimized for sensitivity. Because of the difference in precession frequency, the signal builds up from near zero to reach a maximum, proportional to the applied gradient,

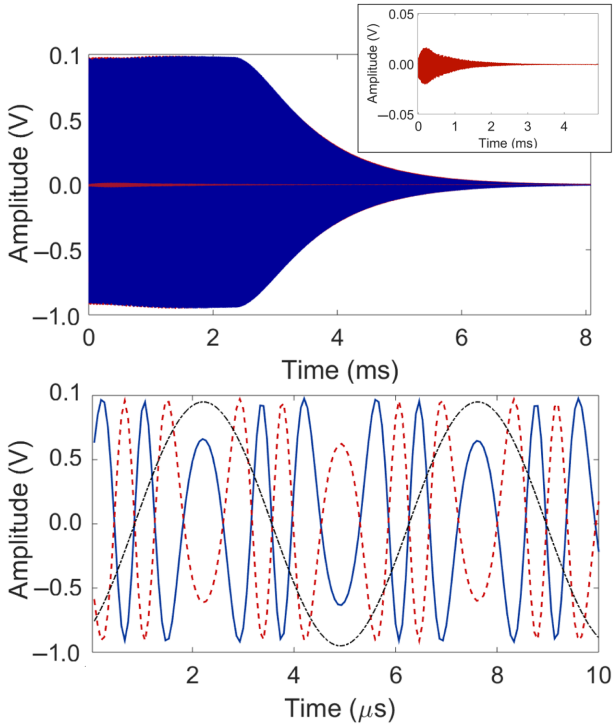

FIG. 2. Experimental signals. Top: Individual (blue) and differential (red) rotation signals at field $B_z = 26$ μT, 400 μW probe power, and 120 °C. The inset shows an enlargement of the differential signal with direct cancellation at near-zero gradient. Bottom: Individual signals over a shorter timescale showing a π phase difference between the $V_{\rm top}$ (solid blue line) and $V_{\rm bot}$ (dashed red line) contributions when the atomic ensembles are polarized with opposite circular polarization. The signals undergo multiple zero crossings over a Larmor period of spin precession (dot-dashed black line).

and then it decays due to relaxation in both contributions. We develop two complementary data-analysis and optimization procedures. In the first strategy, we independently fit the two contributions to get the probe voltage amplitude V_0, initial rotation amplitudes ϕ_0, precession frequencies ν_L, phases ϕ_0, and relaxation times T_2. Because these values typically agree within 1% between top and bottom signals, in Eq. (1) we substitute $\phi_0^{\rm bot} = \phi_0^{\rm top} + \Delta\phi$, $T_2^{\rm bot} = T_2^{\rm top} + \Delta T_2$, and $d_0^{\rm bot} = d_0^{\rm top} + \Delta d_0$ and we perform a third fit to the direct gradiometer signal with $\Delta\nu$, $\Delta\phi$, ΔT_2, and Δd_0 as free parameters to take into account residual variations in all variables. Note that all four variables generate distinct differences in the signal shape and can be determined independently. The frequency difference output $\Delta\nu$ is shown in Fig. 3 as a function of the absolute magnetic field difference $\Delta B = (\partial B_z/\partial y)\Delta y$ generated by the externally applied gradient $\partial B_z/\partial y$, including an offset of about 0.3 nT/cm for zeroing the residual background. The experimental slope is in very good agreement with the nominal gradient coil calibration of 0.55 nT/cm mA

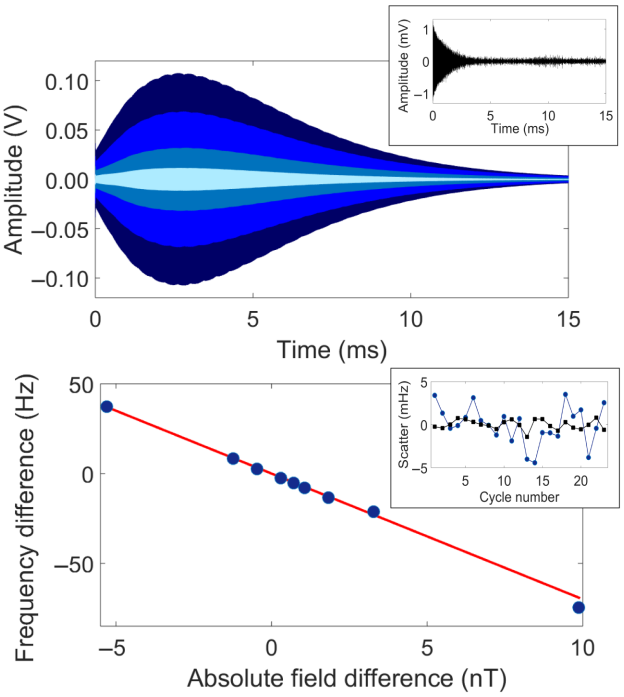

FIG. 3. Top: Finite-gradient gradiometer signal. Gradiometer signal at applied gradients of (from top to bottom) 0.8, 0.5, 0.3, and 0.1 nT/cm. The inset shows the signal in the absence of optical pumping, showing fundamental noise and residual spin excitations. Bottom: Calibration. Experimental (blue points) frequency difference and nominal gradient slope (red line) as a function of applied-magnetic-field difference. The inset shows the frequency-difference scatter over multiple measurements for polarized (blue dots) and unpolarized (black squares) atoms.

and the $\Delta y = 1.4$ cm gradiometer baseline. At a fixed gradient, we perform repeated measurements to obtain the standard deviation in the frequency-difference estimation $\sigma_{\Delta\nu}$ and the differential magnetic sensitivity $B_{\Delta\nu} = (2\pi/\gamma)\sigma_{\Delta\nu}/\sqrt{\Delta f}$, in the unit of teslas per square root hertz, where $\Delta f = 1/(2T_m)$ is the gradiometer bandwidth and $T_m = 2$ ms is the fitting time for each signal, which is chosen for optimal sensitivity [25]. In the inset in the lower part of Fig. 3 we report an optimal experimental scatter with a standard deviation of 2.2 mHz, resulting in a measured sensitivity of 14.2 fT/$\sqrt{\text{Hz}}$, corresponding to a gradiometer sensitivity of 10.1 fT/cm $\sqrt{\text{Hz}}$ for a 1.4-cm baseline. The signal obtained without the pump beam is shown in the inset in the upper part of Fig. 3. It includes spin noise and rf spin excitation of a residual spin polarization created by a slight circular polarization of the probe laser. Use of the same fitting procedure on the residual spin excitation gives a standard deviation of 0.6 mHz, corresponding to a sensitivity of 3.6 fT/$\sqrt{\text{Hz}}$. The latter closely approaches the fundamental value of 2.7 fT/$\sqrt{\text{Hz}}$ obtained by numerical simulations of the signal, given by Eq. (1) with the addition of photon shot noise and atomic spin noise, independently measured as described in detail in the next section.

We also implement a second signal-analysis method that allows real-time measurements of the gradient signal and sensitivity. For small $\Delta\nu$, $\Delta\phi_0$, Δd_0, and ΔT_2, one can expand Eq. (1) to obtain

$$V(t) = V_0\,[2\phi_0(\Delta d_0 + 2\pi\,\Delta\nu t)\cos(2\pi\,\nu_L + d_0) + 2(\Delta\phi_0 + \phi_0\Delta T_2 t/T_2^2)\sin(2\pi\,\nu_L + d_0)]\,e^{-t/T_2}. \tag{2}$$

One can see tha the gradient signal $\Delta\nu$ appears out of phase with respect to the individual top and bottom signals. We perform an appropriately phased FFT on the FID data and look separately at the real and imaginary Fourier components, which each depend on pairs of unknown parameters, $\{\Delta\phi_0,\ \Delta T_2\}$ and $\{\Delta\nu,\ \Delta d_0\}$, respectively. This is done experimentally by our performing FFT on each shot in real time. To optimally extract the signal $\Delta\nu$, we multiply the FID by a custom window function before doing the FFT. Generally the optimal window function to maximize the SNR in the presence of white noise is a matched filter equal to the envelope of the signal [26], in our case $w(t) = (t/T_2)e^{-t/T_2}$. We find that this real-time method gives similar sensitivity to the nonlinear-fitting approach.

IV. NOISE ANALYSIS

When the atomst are polarized in the gradiometer operation mode, the sensitivity is limited by random spin excitations, due to rf broadband noise and pump fluctuations, resulting in a noise amplitude greater than the fundamental atomic noise. In Fig. 4 we report the spin-noise power spectral density (PSD), measured at 120 °C by our probing intrinsic fluctuations of the unpolarized ensemble [28] with a red detuning of 200 GHz from the $F = 2$ state. We also do not apply the $\pi/2$ pulses, so the residual spin polarization of the atoms is not excited. One can see that the peak spin-noise power spectral density exceeds the background-noise power spectral density by more than a factor of 10, indicating good quantum-nondemolition resolution of the multipass cell. The spin-noise power spectrum is given by $S(\nu) = \langle\phi(t)^2\rangle\int_{-\infty}^{\infty} C(|\tau|)e^{-i2\pi\nu\tau}d\tau$, where $C(|\tau|) = C_d(\tau)e^{-\tau/T_2}$ is the normalized spin-noise time-correlation function, set by spin relaxation processes and the diffusion correlation function $C_d(\tau)$. The latter, which was derived analytically in Ref. [23] for an arbitrary probe geometry, can modify the spectral lineshape, while it does not affect the total rotation noise variance $\langle\phi(t)^2\rangle$. For 60 passes through a 1-cm-long Rb vapor with measured density $n = 1.75\times10^{13}$ cm^{-3}, we calculate theoretical optical rotation rms noise $\phi_{\text{rms}}^{\text{theor}}$ of 3.6×10^{-6} rad [29]. This is in good agreement with the measured area under the noise peak $\phi_{\text{rms}}^{\text{expt.}} = 3.8\times10^{-6}$ rad after subtraction of the background-noise floor of $\phi_{\text{ph}} = 3.7\times10^{-8}$ rad/$\sqrt{\text{Hz}}$.

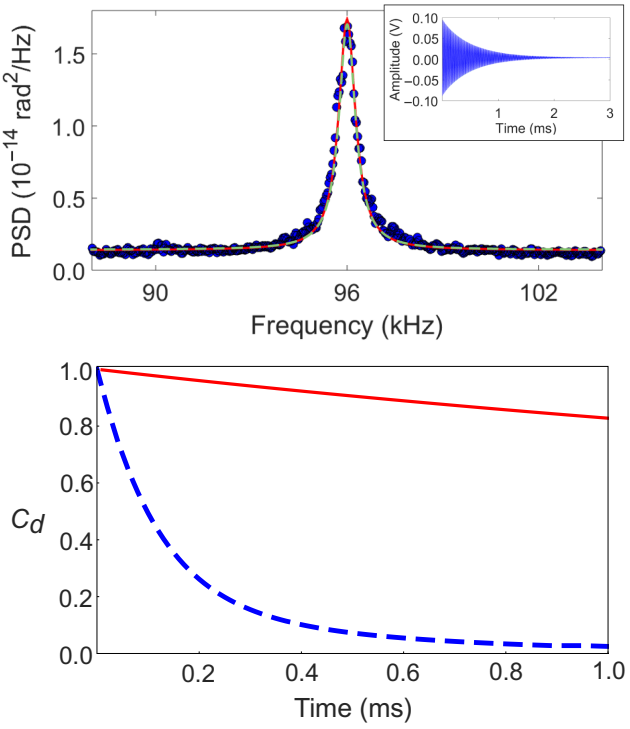

FIG. 4. Top: Spin-noise spectrum. Experimental spin-noise spectrum (blue points) centered at Larmor frequency $\nu_L = 96$ kHz and a simple Lorentzian fit (red line) for an unpolarized atomic ensemble under thermal equilibrium at 120 °C. Prediction for the spin-noise spectrum including effects of diffusion without free parameters (dashed green line) The inset shows the free-induction-decay signal for low initial polarization, where spin-exchange collisions limit the transverse relaxation time. Bottom: Comparison of diffusion correlation functions. Calculated diffusion correlation function for the V-shaped multipass cell (red line) in comparison with the diffusion correlation function for the cylindrical-mirror multipass cavity [27] used in Ref. [16].

If the noise peak is fit to a Lorentzian (shown by a red line in Fig. 4), it gives a full width at half maximum of 640 Hz. The transverse relaxation time T_2 of a small coherent excitation obtained in the regime of low spin polarization, shown in the inset in Fig. 4, is 0.55 ms, which corresponds to a full width at half maximum of $1/\pi T_2 =$ 580 Hz. The difference between the two linewidths is due to effects of atomic diffusion on the spin-noise spectrum. However, because of the overlapping of multiple probe beams with a uniform diameter of 3.6 mm, the spectrum has nearly a pure-Lorentzian shape, in contrast to prior work with multipass cells, where, due to different transit times and varying probe focusing, the spin-noise linewidth was limited by atomic diffusion, resulting in a distribution of Lorentzian functions [16,20]. In the regime where the probe-beam Rayleigh range is much larger than the length of the atomic vapor, the diffusion correlation function is given by $C_d^{\text{theor}}(t) = 1/(1 + 4tD/w_0^2)$ [23], where D is the diffusion constant and w_0 is the Gaussian beam radius ($D = 1.5$ cm^2/s and $w_0 = 1.8$ mm in our cell). The expected spin-noise spectrum is given by Eq. (17) in Ref. [23], and is shown by a dashed green line in Fig. 4 for $T_2 = 0.55$ ms. One can see excellent agreement with the measured spectrum without any free parameters. To illustrate the difference in the diffusion correlation functions, we show in Fig. 4 a comparison of the correlation function in the present experiment and in our prior multipass-cavity design [16]. The multipass design described, in addition to the high optical depth, provides a fundamental advantage with the possibility of increasing the long-term sensitivity by spin squeezing [30], because quantum correlations [18,31] could be preserved in a dense vapor despite atomic diffusion.

V. CONCLUSIONS

We introduce a direct magnetic gradiometer showing a near-zero signal despite the high optical rotation introduced by two atomic ensembles. The sensor consists of a single multipass cell, in contrast to prior geometries based on either two vapor cells or two output signals [32]. The intrinsic cancellation of large polarization rotations, which is typical in state-of-the-art optical magnetometry, avoids complications related to signal processing. We develop two analysis methods for the special signal, and we measure a sensitivity of 10.1 fT/cm $\sqrt{\text{Hz}}$ with a 1.4-cm baseline and femtotesla projected sensitivity. The described gradiometer is also a multipass atomic sensor with a nearly-pure-Lorentzian spin-noise spectrum, where atomic diffusion does not significantly affect the time correlation of the spin noise [16,20]. In a quantum-noise-limited regime this would allow suppression of atomic spin noise due to spin squeezing [31,33], while the sensitivity could be further increased by useof a squeezed-light probe [34,35]. While the V-shaped-cell gradiometer described has not yet been tested in an unshielded environment, we expect that it will work particularly well for cancellation of broadband magnetic noise since it relies on direct real-time subtraction of two signals. We have successfully used an alternative approach based on two independent frequency measurements in multipass cells for operation in an unshielded environment [14], but we found it to suffer from reduced sensitivity in the presence of high-frequency magnetic noise. Therefore, a direct gradiometer is more promising for applications in challenging environments [36]. Finally, because of the anodic bonding fabrication technique, it could be further miniaturized [37].

ACKNOWLEDGMENTS

This work was supported by the DARPA AMBIENT program.

[1] Elena Boto, Niall Holmes, James Leggett, Gillian Roberts, Vishal Shah, Sofie S. Meyer, Leonardo Duque Muñoz, Karen J. Mullinger, Tim M. Tierney, Sven Bestmann, Gareth R. Barnes, Richard Bowtell, and Matthew J. Brookes, Moving magnetoencephalography towards real-world applications with a wearable system, Nature **555**, 657 (2018).

[2] Kasper Jensen, Rima Budvytyte, Rodrigo A. Thomas, Tian Wang, Annette M. Fuchs, Mikhail V. Balabas, Georgios Vasilakis, Lars D. Mosgaard, Hans C. Stærkind, Jörg H. Möller, Thomas Heimburg, Søren-Peter Olesen, and Eugene S. Polzik, Non-invasive detection of animal nerve impulses with an atomic magnetometer operating near quantum limited sensitivity, Sci. Rep. **6**, 29638 (2016).

[3] Zhaoqiang Chu, Huaduo Shi, Mohammad Javad PourhosseiniAsl, Jingen Wu, Weiliang Shi, Xiangyu Gao, Xiaoting Yuan, and Shuxiang Dong, A magnetoelectric flux gate: New approach for weak dc magnetic field detection, Sci. Rep. **7**, 8592 (2017).

[4] Andrew David, Mark Cole, Tim Horsley, Neil Linford, Paul Linford, and Louise Martin, A rival to stonehenge? Geophysical survey at stanton drew, England, Antiquity **78**, 341 (2004).

[5] M. N. Nabighian, V. J. S. Grauch, R. O. Hansen, T. R. LaFehr, Y. Li, J. W. Peirce, J. D. Phillips, and M. E. Ruder, The historical development of the magnetic method in exploration, Geophysics **70**, 33ND (2005).

[6] H. H. Nelson and J. R. McDonald, Multisensor towed array detection system for uxo detection, IEEE Trans. Geosci. Remote Sens. **39**, 1139 (2001).

[7] Dmitry Budker and Michael Romalis, Optical magnetometry, Nat. Phys. **3**, 227 (2007).

[8] J. C. Allred, R. N. Lyman, T. W. Kornack, and M. V. Romalis, High-Sensitivity Atomic Magnetometer Unaffected by Spin-Exchange Relaxation, Phys. Rev. Lett. **89**, 130801 (2002).

[9] I. K. Kominis, T. W. Kornack, J. C. Allred, and M. V. Romalis, A subfemtotesla multichannel atomic magnetometer, Nature **422**, 596 (2003).

[10] H. B. Dang, A. C. Maloof, and M. V. Romalis, Ultrahigh sensitivity magnetic field and magnetization measurements with an atomic magnetometer, Appl. Phys. Lett. **97**, 151110 (2010).

[11] S. J. Smullin, I. M. Savukov, G. Vasilakis, R. K. Ghosh, and M. V. Romalis, Low-noise high-density alkali-metal scalar magnetometer, Phys. Rev. A **80**, 033420 (2009).

[12] V. G. Lucivero, W. Lee, M. V. Romalis, M. E. Limes, E. L. Foley, and T. W. Kornack, in *Quantum Information and Measurement (QIM) V: Quantum Technologies*, Rome, Italy, OSA Technical Digest (Optical Society of America, 2019), paper T3C.3. https://doi.org/10.1364/qim.2019.t3c.3.

[13] D. Sheng, A. R. Perry, S. P. Krzyzewski, S. Geller, J. Kitching, and S. Knappe, A microfabricated optically-pumped magnetic gradiometer, Appl. Phys. Lett. **110**, 031106 (2017).

[14] M. E. Limes, E. L. Foley, T. W. Kornack, S. Caliga, S. McBride, A. Braun, W. Lee, V. G. Lucivero, and M. V. Romalis, Portable Magnetometry for Detection of Biomagnetism in Ambient Environments, Phys. Rev. Appl. **14**, 011002 (2020).

[15] Rui Zhang, Rahul Mhaskar, Ken Smith, and Mark Prouty, Portable intrinsic gradiometer for ultra-sensitive detection of magnetic gradient in unshielded environment, Appl. Phys. Lett. **116**, 143501 (2020).

[16] D. Sheng, S. Li, N. Dural, and M. V. Romalis, Subfemtotesla Scalar Atomic Magnetometry Using Multipass Cells, Phys. Rev. Lett. **110**, 160802 (2013).

[17] Joonas Iivanainen, Rasmus Zetter, Mikael Grön, Karoliina Hakkarainen, and Lauri Parkkonen, On-scalp meg system utilizing an actively shielded array of optically-pumped magnetometers, NeuroImage **194**, 244 (2019).

[18] W. Wasilewski, K. Jensen, H. Krauter, J. J. Renema, M. V. Balabas, and E. S. Polzik, Quantum Noise Limited and Entanglement-Assisted Magnetometry, Phys. Rev. Lett. **104**, 133601 (2010).

[19] Keigo Kamada, Yosuke Ito, Sunao Ichihara, Natsuhiko Mizutani, and Tetsuo Kobayashi, Noise reduction and signal-to-noise ratio improvement of atomic magnetometers with optical gradiometer configurations, Opt. Express **23**, 6976 (2015).

[20] S. Li, P. Vachaspati, D. Sheng, N. Dural, and M. V. Romalis, Optical rotation in excess of 100 rad generated by rb vapor in a multipass cell, Phys. Rev. A **84**, 061403 (2011).

[21] Herbert Crepaz, Li Yuan Ley, and Rainer Dumke, Cavity enhanced atomic magnetometry, Sci. Rep. **5**, 15448 (2015).

[22] S. Appelt, A. Ben-Amar Baranga, A. R. Young, and W. Happer, Light narrowing of rubidium magnetic-resonance lines in high-pressure optical-pumping cells, Phys. Rev. A **59**, 2078 (1999).

[23] V. G. Lucivero, N. D. McDonough, N. Dural, and M. V. Romalis, Correlation function of spin noise due to atomic diffusion, Phys. Rev. A **96**, 062702 (2017).

[24] For high initial polarization, the decay can be nonexponential due to partial spin-exchange-relaxation suppression [16]. Furthermore, Eq. (1) is valid and has been tested at finite fields where the nonlinear Zeeman effect is negligible.

[25] C. Gemmel, W. Heil, S. Karpuk, K. Lenz, Ch. Ludwig, Yu. Sobolev, K. Tullney, M. Burghoff, W. Kilian, S. Knappe-Grüneberg, W. Müller, A. Schnabel, F. Seifert, L. Trahms, and St. Baeßler, Ultra-sensitive magnetometry based on free precession of nuclear spins, Eur. Phys. J. D **57**, 303 (2010).

[26] Richard G. Spencer, Equivalence of the time-domain matched filter and the spectral-domain matched filter in one-dimensional nmr spectroscopy, Concepts Magn. Reson. **36A**, 255 (2010).

[27] Joel A. Silver, Simple dense-pattern optical multipass cells, Appl. Opt. **44**, 6545 (2005).

[28] B. Aleksandrov and V. S. Zapasskii, Magnetic resonance in the faraday-rotation noi spectrum, Sov. Phys. JETP **54**, 64 (1981).

[29] V. Shah, G. Vasilakis, and M. V. Romalis, High Bandwidth Atomic Magnetometery with Continuous Quantum Nondemolition Measurements, Phys. Rev. Lett. **104**, 013601 (2010).

[30] G. Vasilakis, V. Shah, and M. V. Romalis, Stroboscopic Backaction Evasion in a Dense Alkali-Metal Vapor, Phys. Rev. Lett. **106**, 143601 (2011).

[31] Jia Kong, Ricardo Jiménez-Martínez, Charikleia Troullinou, Vito Giovanni Lucivero, Géza Tóth, and Morgan

W. Mitchell, Measurement-induced, spatially-extended entanglement in a hot, strongly-interacting atomic system, Nat. Commun. **11**, 2415 (2020).

[32] A. R. Perry, M. D. Bulatowicz, M. Larsen, T. G. Walker, and R. Wyllie, An all-optical atomic gradiometer with sub-20 ft/cm/$\sqrt{\text{Hz}}$ sensitivity in a 22 μT earth-scale magnetic field, arXiv:2008.13234 (2020).

[33] Han Bao, Junlei Duan, Shenchao Jin, Xingda Lu, Pengxiong Li, Weizhi Qu, Mingfeng Wang, Irina Novikova, Eugeniy E. Mikhailov, Kai-Feng Zhao, Klaus Mølmer, Heng Shen, and Yanhong Xiao, Spin squeezing of 1011 atoms by prediction and retrodiction measurements, Nature **581**, 159 (2020).

[34] Vito Giovanni Lucivero, Ricardo Jiménez-Martínez, Jia Kong, and Morgan W. Mitchell, Squeezed-light spin noise spectroscopy, Phys. Rev. A **93**, 053802 (2016).

[35] Vito Giovanni Lucivero, Aleksandra Dimic, Jia Kong, Ricardo Jiménez-Martínez, and Morgan W. Mitchell, Sensitivity, quantum limits, and quantum enhancement of noise spectroscopies, Phys. Rev. A **95**, 041803 (2017).

[36] KaiMei C. Fu, Geoffrey Z. Iwata, Arne Wickenbrock, and Dmitry Budker, Sensitive magnetometry in challenging environments, arXiv:2008.00082 (2020).

[37] John Kitching, Chip-scale atomic devices, Appl. Phys. Rev. **5**, 031302 (2018).